Discharge coefficient of an orifice jet in cross flow: influence of inlet conditions and optimum velocity ratio

Sandrine Berger*, Nicolas Gourdain †, and Michaël Bauerheim‡
ISAE-SUPAERO, Université de Toulouse, 31400 Toulouse, France

Sébastien Devillez§
LATECOERE, 31500 Toulouse, France

The present work aims to characterize the discharge performance of aircraft door vent flaps. For this purpose, three different configurations with increasing complexity are studied with a RANS and a LES solver. The first configuration consists of an orifice plate in a duct for which experimental pressure loss data are available in the literature. This configuration is used as a reference for the validation of the RANS and LES setups. The duct placed downstream of the orifice is then removed to produce an unconfined geometry in which the orifice jet discharges either into an open atmosphere or a transverse flow. Finally, a classic jet in cross flow is also studied. The main objective is to analyze the discharge coefficient variations depending on three key parameters: (i) the jet Reynolds number, (ii) the inlet velocity profile, and (iii) the velocity ratio between the jet and the cross flow. Results show that for cases without cross flow, the jet Reynolds number has no influence on the discharge performance whereas a steady decrease of the orifice pressure loss is observed as the duct inlet velocity profile is deformed from that of a flat profile. The Poiseuille profile is found to minimize the pressure loss. In addition, numerical data of the reference configuration compare well with experimental values when such a profile is prescribed. Finally, simulations with a cross flow evidence an optimal velocity ratio for which the discharge coefficient is maximum and exceeds the freejet value.

I. Nomenclature

C_d	=	discharge coefficient
d	=	orifice diameter
e	=	orifice plate thickness
h	=	duct side length
k	=	discharge coefficient
Ma_{jet}	=	Jet Mach number
$\dot{m}_{eff}$	=	effective mass flow rate extracted from the simulation
$\dot{m}_{ideal}$	=	ideal isentropic mass flow rate
P_d	=	dynamic pressure
P_{ref}	=	reference static pressure
P_s	=	static pressure
Re_{jet}	=	jet Reynolds number (based on orifice diameter and jet bulk velocity)
R_v	=	velocity ratio
S	=	orifice area
T	=	temperature
U_{in}, U_{jet}, U_{CF}	=	inlet, jet, and cross flow bulk velocities respectively
U_x	=	axial component of the velocity field
ρ	=	density

*Postdoctoral Researcher, Département Aérodynamique et Propulsion, 10 av Édouard-Belin BP 54032, 31055 Toulouse Cedex 4, France.
†Professor, Département Aérodynamique et Propulsion, 10 av Édouard-Belin BP 54032, 31055 Toulouse Cedex 4, France.
‡Associate Professor, Département Aérodynamique et Propulsion, 10 av Édouard-Belin BP 54032, 31055 Toulouse Cedex 4, France.
§R&T Doors Product Architect, Innovation and R&T Department, 135 Rue de Périole BP 25211, 31079 Toulouse Cedex 5, France.

II. Introduction

Outward-opening aircraft doors are equipped with vent flaps which can vent air to the freestream to prevent cabin pressurization if the door latching system is not properly engaged. In the absence of such safety systems, the unsecured door may be "blown open" by the pressure inside the cabin, leading to rapid or explosive decompression. Such uncontrolled decompression can harm passengers, damage aircraft components, and has caused accidents in the past [1]. To avoid these dangerous events, current aviation regulations require the installation of a "pressure prevention mean". Such a device must preclude the difference between cabin pressure and external pressure (usually called cabin differential pressure) exceeding 3447 Pa, or equivalently 0.5 psi, if the door locking system is not completely engaged. To match this requirement, the vent flap solution consists of creating an opening in the door equipped with a mobile vent panel (Fig. 1). Mechanically, the panel can only close when the door latching system is secured. The size of this opening

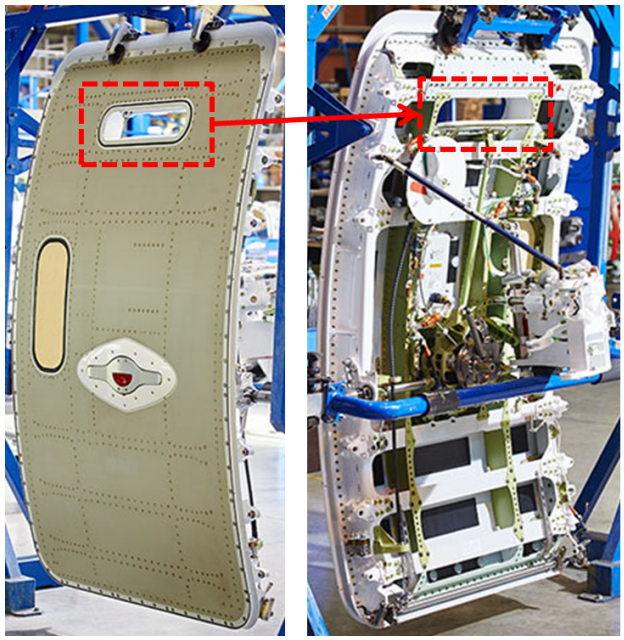

(a) Pictures of passengers door designed and produced by LATECOERE. From www.latecoere.aero.

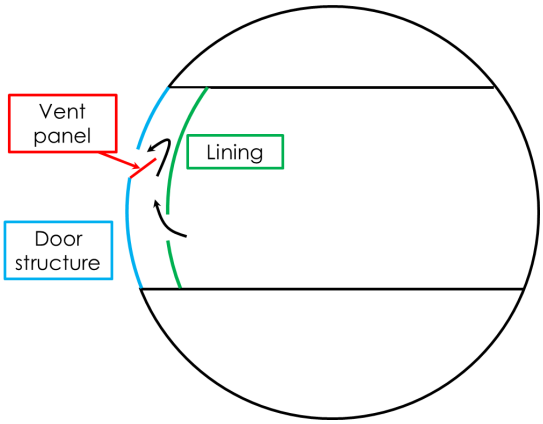

(b) Scheme of air evacuation from the cabin to the door vent flap.

Fig. 1 Illustrations of the door vent flap system.

determines the structural layout of the door and is therefore critical for its design. The larger it is, the more constraining this element is for the design of the rest of the door. Therefore, designers need to define the minimum opening size for sufficient air ejection to maintain cabin differential pressure below the required limit. To do so, flow pressure losses through the lining opening, the various mechanisms installed inside the door and the door opening (Fig. 1) need to be determined. As a first step, only the latter is analyzed here.

Within this scope, some results from the literature are of special interest. Current door vent flap designs are usually based on the experimental data produced in the 1950s by NACA [2, 3] and which provide discharge coefficients for air outlets discharging into a transonic flow. Air outlets of various geometries are studied in these publications. In particular, the investigation of flush outlets leads to the following observations:

- The discharge coefficient increases with mass flow ratio between the outlet jet and the cross flow, approaching a free jet condition or even exceeding its value in some cases.
- For circular thin plate outlets, the discharge coefficient evolution with mass flow ratio appears to approach a maximum at the higher mass flow ratios investigated. Moreover, for rectangular thin plate outlets of high aspect ratio and with the longer side placed parallel to the cross flow, an optimum discharge coefficient is clearly in evidence. The corresponding mass flow ratio decreases when aspect ratio increases.
- At high flow rates, discharge coefficients of circular outlets are increased by the addition of a bellmouthed section ahead of the opening

- Finally, whatever the outlet, the influence of the cross flow Mach number is limited, in the range covered by the tests (between 0.7 and 1.3).

One geometry for which experimental data are reported in [3], was later investigated numerically in [4]. In this publication, CFD (Computational Fluid Dynamics) results for the discharge coefficient reproduce experimental results from [3] with a maximum deviation of 10%. In addition, the authors observed very close values for the discharge coefficient when the cross flow Mach number was equal to 0.7 and 0.3. Note that, following the regulations for the design of the "pressure prevention mean" and based on current door vent flap designs, the jet Reynolds and Mach numbers to be considered are of the order of 5×10^5 and 0.15 respectively while the outside air Mach number is between 0 and 0.6.

From a more academic point of view, the problem considered in this paper is the combination of two classical problems of fluid mechanics: the orifice plate in a duct and the Jet In Cross Flow (JICF). As evidenced by a recent review on JICF [5], literature on this configuration is abundant but mostly focused on the flow field downstream of the jet exit and data on pressure loss are not reported. When such data are made available, the target application is generally dedicated to the cooling of hot stages of aeronautical engines [6–9] for which the configurations are too far from the present problem to extrapolate the conclusions directly. Regarding studies on orifice plates placed in a duct, there is a greater body of work relevant to the present study. In particular, the effect of inlet velocity profile deformation is a well known issue for orifice flow meters accuracy [10–15]. Some publications evidenced numerically [12] and experimentally [11, 13] a significant influence of axial deformations of the upstream velocity profile on the discharge coefficient of an orifice at a Reynolds number of 5×10^4. This result suggests that in the door vent flap case, the flow inside the door and the position and opening angle of the vent panel are of great importance in the determination of the pressure losses through the opening. Another orifice flow study published in [16], provides experimental pressure loss data for Mach and Reynolds numbers very close to those encountered in the aircraft door vent flap problem. This data are therefore used in the current work to validate the various numerical tools.

Flow pressure loss through door vent flaps is analyzed in this paper with three different configurations of increasing complexity, (Fig. 2). The reference configuration, consisting of an orifice plate in a duct (Fig. 2a) and for which

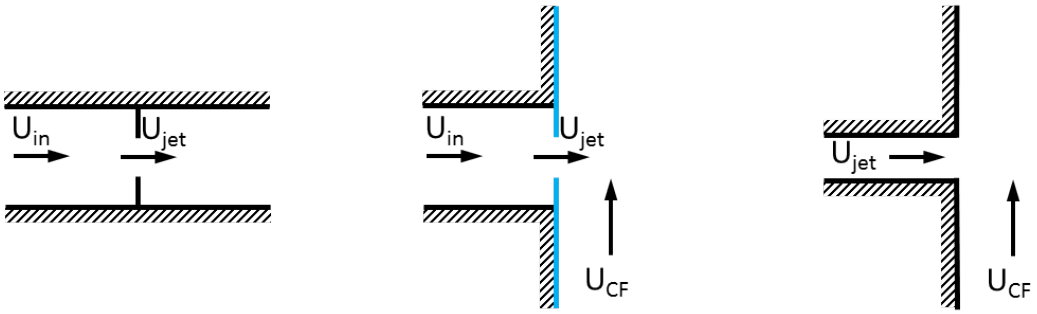

(a) Reference **(b) Orifice-unconfined** **(c) JICF**

Fig. 2 Configurations studied in this publication.

experimental data are available [16], is first studied and used to validate the numerical tools. The duct placed downstream of the orifice is then removed to produce an orifice-unconfined geometry (Fig. 2b) in which the orifice jet discharges either into an open atmosphere or a transverse flow of velocity U_{CF}. Finally, a JICF configuration (Fig. 2c) is computed to isolate the contributions from the orifice and from the cross flow in the orifice-unconfined case. The discharge coefficient associated to the three cases is analyzed as well as discharge performance variations with jet Reynolds number, inlet velocity profile, and velocity ratio between the jet and the cross flow. The reference configuration is investigated in section Section III of this paper while both unconfined cases are investigated in the section Section IV.

III. Reference configuration

The configuration experimentally investigated in [16] is computed with two numerical methods: a Reynolds Average Navier Stokes (RANS) solver Star-CCM+ and a Large Eddy Simulation (LES) code IC3. The geometry as well as the numerics of each solver are first detailed. A general description of the flow is then proposed, and the orifice pressure loss is finally analyzed and compared to experimental results.

A. Configuration

The validation configuration is illustrated in Figs. 2a and 3. It consists of a plate of thickness $e = 0.002\ m$, pierced with a circular orifice of diameter $d = 0.239\ m$, and placed in a square duct which sides measure $h = 0.3\ m$. Air flows in the duct from left to right. The blocking ratio imposed on the flow by the obstacle is $\frac{\pi d^2/4}{h^2} = 0.5$. The channel length is set to $3h$ upstream and $10h$ downstream of the orifice. Note that the duct length is not given in [16]. A specific study has therefore been performed with the solver Star-CCM+ to ensure that the results remain unchanged when increasing the upstream and downstream lengths. As indicated in Fig. 3, the x-axis is oriented in the flow direction, from left to right, and the y and z coordinates in the transverse directions. The origin of the axes is located on the upstream face of the plate, at the orifice center.

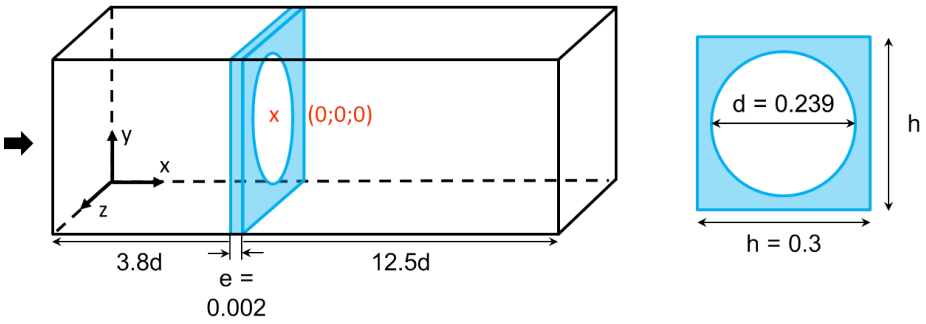

Fig. 3 Schematic view of the reference configuration. Dimensions are given in meters.

In [16], the orifice discharge coefficient k is measured for jet Reynolds numbers (based on the orifice diameter and jet bulk velocity) ranging from $Re_{jet} = 1.6 \times 10^5$ to $Re_{jet} = 3.7 \times 10^5$. Considering classical experimental conditions (not given in [16]), this corresponds to a Mach number range from $Ma_{jet} = 0.03$ to $Ma_{jet} = 0.07$. Since additional measurements of the static pressure at various locations along the duct wall are given for the case $Re_{jet} = 3.2 \times 10^5$, the latter is used for comparison between experimental and numerical data.

Some uncertainties remain concerning the conditions under which this experiment was carried out:

- The temperature, pressure, and density of the fluid are not specified by the authors. The following classical values were therefore used: $P_{ref} = 101325\ Pa$, $T = 294.15\ K$ and $\rho = 1.2\ kg.m^{-3}$. Nevertheless, the Mach number being very small, the experiment can be considered as incompressible, limiting the impact of these values.
- The velocity profile is unknown which is particularly problematic at the duct inlet. A sensitivity study of the inlet profile on the discharge coefficient is hence conducted in III.D.

Boundary conditions are as follows. At the inlet, air is injected in the x direction with a bulk velocity equal to $U_{in} = 9.83\ m.s^{-1}$ and various velocity profiles. The fluid temperature and density are set to $T = 294.15\ K$ and $\rho = 1.2\ kg.m^{-3}$ respectively. The outlet condition is set so that the mean pressure on the boundary is equal to the atmospheric pressure minus the inlet dynamic pressure and the pressure drop measured in [16], leading to $P_s^{outlet} = 101078\ Pa$. The thin plate walls as well as the orifice walls are prescribed with no-slip conditions (blue in Fig. 3). Finally, in order to suppress pressure losses due to fluid-wall friction along the duct walls, these are defined as slip walls.

B. Numerical methods

1. The RANS solver Star-CCM+

Star-CCM+ [17] is a numerical platform developed by Siemens PLM Software. The results presented in this paper have been obtained by solving the incompressible RANS equations with a finite volume method. The convective terms are solved thanks to a second order upwind scheme, and the turbulent terms are taken into account with the kω-SST model [18, 19]. A sensitivity study to the turbulence model has been conducted with two additional turbulence models: kϵ-v2f [20, 21] and Spalart-Allmaras [22]. The results indicated low variations of the orifice pressure drop with the model. These were below 5% which is lower than the global measurements uncertainties estimated in [16]. All computations are initialized with uniform fields equal to the inlet velocity and the outlet pressure.

To reduce the cost of the simulations, only one quarter of the full domain is computed because of the symmetries of the problem. Solutions obtained from the computation of the full and the reduced domains were compared and gave identical results. The CFD domain is discretized with a hexahedral 3D mesh which is refined near the orifice, both in the main flow and the transverse directions. Mesh convergence is assessed through comparison of the results obtained on three different meshes, and with a flat velocity profile at the duct inlet. Mr0 is the reference mesh. Mr1 is refined in the orifice thickness (x direction) as well as near the orifice wall (yz plane). Mr2 offers an additional level of refinement at the same locations. To ensure a suitable mesh quality for the RANS computations, cell size is adapted in the whole domain for all three meshes. The cells aspect ratio does not exceed 500 in the domain overall, and is limited to 20 in the areas of interest. The inflation factor is limited to 1.1. Characteristics of the three meshes are detailed in Table 1.

	Mr0	Mr1	Mr2
Number of cells	850 000	$1.5M$	$5.1M$
Mean y^+	47	1.8	0.75
Maximum y^+	89	4	2.6
Ratio between current mesh and Mr0 CPU costs	1	1.84	3.75
Pressure loss coefficient k	4.52	4.54	4.53

Table 1 Characteristics of the three meshes tested $Mr0$, $Mr1$ and $Mr2$.

y^+ values are one order of magnitude smaller in Mr1 and Mr2 compared to the ones encountered in Mr0. To investigate the potential impact of such differences on pressure loss prediction, the dimensionless static pressure ($\frac{P_s - P_{ref}}{P_d}$) along the channel is plotted for three different lines in Fig. 4. The first line corresponds to the centerline of the duct, the second one is located along the channel walls in the symmetry plane, and the third line runs along the orifice edge. Figure 4 shows that whatever the region of observation, the three meshes provide similar values. The same conclusion arises from the pressure loss coefficient values given in Table 1. These results reveal that the pressure loss is independent of the boundary layers resolution, and Mr0 resolution is sufficient. This mesh is therefore retained for future computations.

2. The LES solver IC3

IC3 is a Large Eddy Simulation (LES) / Direct Numerical Simulation (DNS) research code that solves the unsteady compressible Navier-Stokes equations through a finite volume formulation on unstructured meshes. In all the present simulations, a third order Runge-Kutta method (RK3) is employed for the explicit temporal integration, and convective terms are solved with a second order centered scheme. Subgrid scales are taken into account using the Vreman turbulent viscosity model [23]. Inlet and outlet conditions are prescribed through partially reflective characteristic conditions. Additionally, to improve the simulation robustness, a relaxation coefficient equal to 0.1 between the internal and imposed pressures is added at the outlet. The flow field is initialized with uniform values, or LES solutions obtained on coarser meshes. The computational domain is reduced to a quarter, as with the RANS simulations and mesh convergence has been confirmed following the methodology used for RANS computations.

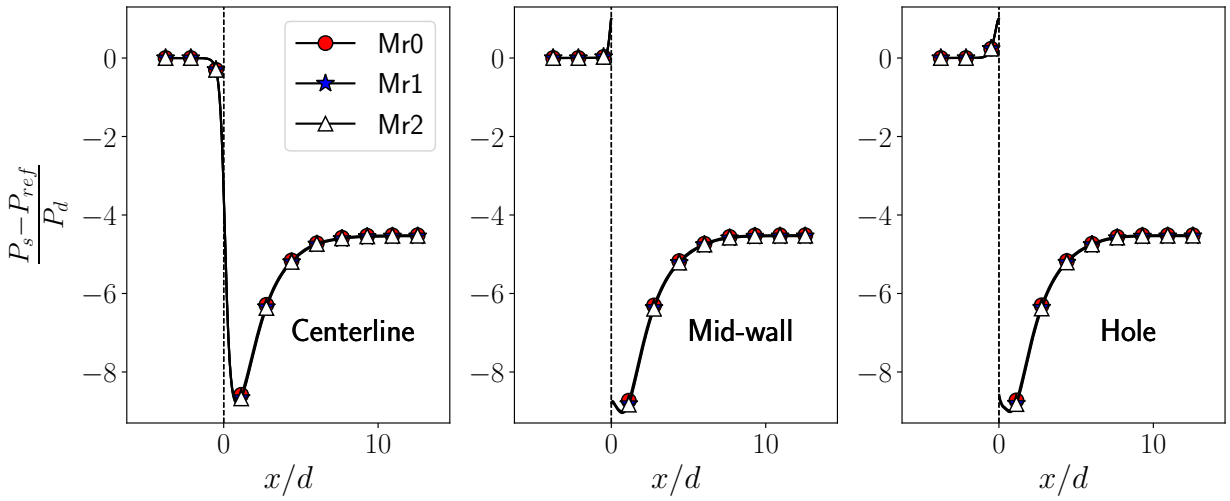

Fig. 4 Spatial evolution of the dimensionless static pressure along the duct for the three meshes tested $Mr0$, $Mr1$, and $Mr2$.

C. Flow description and comparison of RANS and LES fields obtained with a flat inlet velocity profile

To begin with, the flow distribution in the duct is described based on RANS and LES results obtained with a flat inlet velocity profile. In the following, all physical quantities are taken from mean solutions. The flow topology is analyzed in Figs. 5 and 7 on two different 2D cuts of the flow fields : the diagonal plane that passes through the origin, and an axial cut located one diameter downstream of the orifice ($x = d$). Note that duct upstream and downstream lengths are actually longer than the portion shown on the figures.

Figure 5 shows the RANS and LES axial velocity fields U_x in the two cut planes along with zero velocity contours. At the duct inlet, the velocity is uniform over the whole channel height (not shown). The streamlines then bend towards the center due to the passage restriction imposed by the orifice plate, and the axial velocity increases close to the centerline. Downstream of the plate, the orifice jet contracts and accelerates in the axial direction to the well established point of vena contracta. In the outer region of the duct, a large recirculation zone develops. As can be observed in Fig. 5b and 5d, the initially circular jet flattens under the effect of the recirculation zone. This particular topology results from a balance between the high-speed circular jet that naturally spreads and the strong confinement (blocking ratio equal to 0.5) imposed by the squared duct which maintains the recirculation zone close to the jet. Further downstream, the radial extent of the recirculation zone decreases and the central jet expands towards the duct walls. The flow then re-orients in the axial direction due to the constraint imposed by the duct.

The axial velocity fields obtained with RANS (Figs. 5a and 5b) and LES (Figs. 5c and 5d) are very similar upstream of the orifice whereas significant differences can be observed on the downstream side. The jet core and the recirculation zone are shorter in the LES solution, the former being approximately $1/3$ less extended than in the RANS results. As a result, in the LES, the central jet expansion starts further upstream in the channel. In addition, the jet core extremity shape is sharper in the RANS computations.

Differences between RANS and LES solutions are then illustrated in Fig. 6 which presents axial velocity profiles at various locations indicated with vertical lines in Fig. 5. For axial locations up to $x = 0.1d$, both numerical approaches give identical results: the velocity profile curved towards the centerline at $x = -0.1d$, the reverse flow close to the orifice wall at $x = 0.002$ and the recirculation as well as the velocity surge at the jet external extremity at $x = 0.1d$. However, differences between LES and RANS solutions arise at $x = 1d$ and $x = 3d$. At $x = 3d$, close to the duct walls, the axial velocity is negative in RANS and positive in LES, further evidencing a shorter recirculation in the LES solution. The reduced sizes of the jet core and the recirculation in the LES results in a flatter profile than that obtained from the RANS computation at the same location.

Finally, RANS and LES turbulent kinetic energy, TKE, fields are compared in Fig. 7. Once again, both solutions

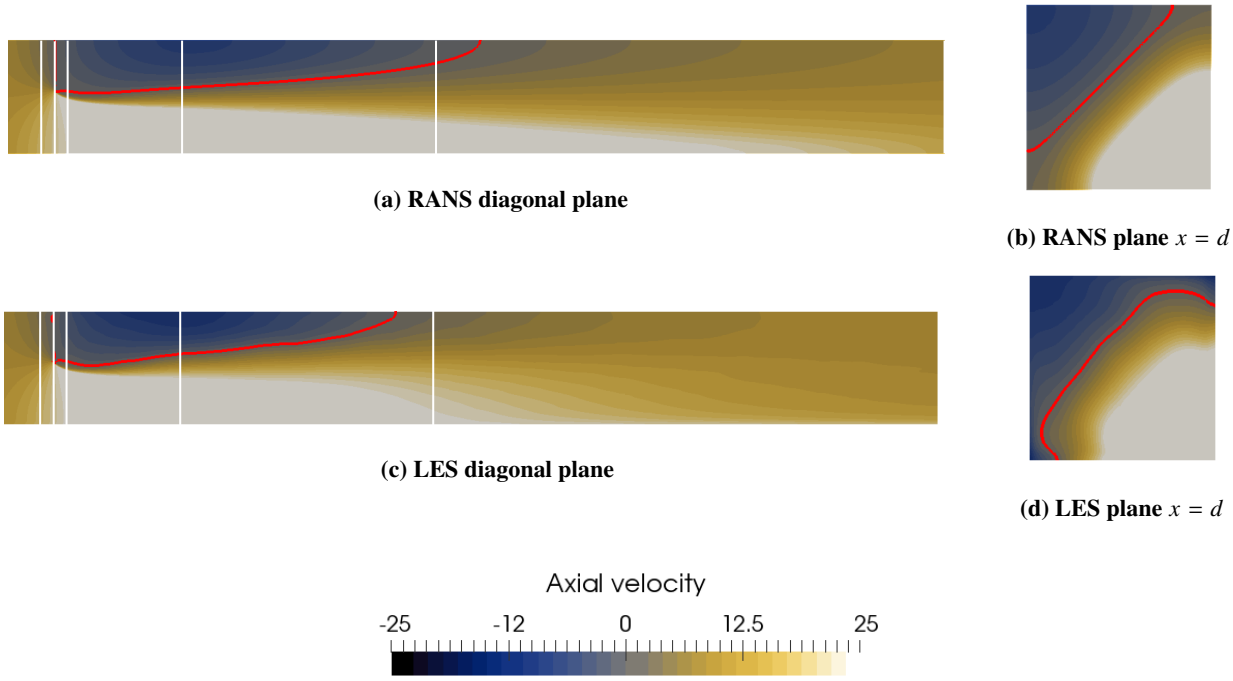

(a) RANS diagonal plane

(b) RANS plane $x = d$

(c) LES diagonal plane

(d) LES plane $x = d$

Fig. 5 Cuts of the axial velocity field U_x and zero axial velocity contours (in red).

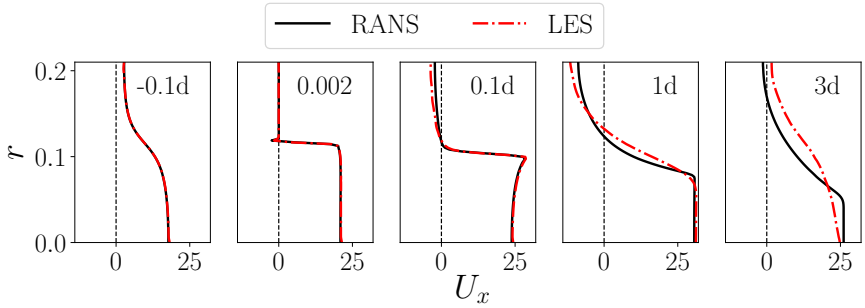

Fig. 6 Axial velocity U_x profiles in the diagonal plane, at various axial locations indicated in Fig. 5.

present similar global features. Turbulence arises mainly from the separation zone between the jet and the recirculation. TKE is at a maximum close to the diagonal plane in the area where both the jet and the recirculation zone are well developed and interact a lot (Figs. 7b and 7d). This zone is however more extended in the LES solution. The LES TKE field is also shifted in the upstream direction compared to RANS, which is consistent with previous observations on the velocity field (Figs. 5a and 5c). In addition, the LES solution shows an additional feature compared to the RANS field: a zone of moderate turbulent kinetic energy lies close to the central line at the location where the jet core "vanishes" (Fig. 5c). This difference may come from the variation in the jet core shape previously observed in Figs. 5a and 5c.

To conclude, RANS and LES provide very similar mean fields upstream of the orifice whereas significant differences can be observed on the downstream part of the duct. In particular, LES field patterns are similar to the RANS one but shifted in the upstream direction with shorter jet core and recirculation zone. Such differences could lead to discrepancies in the pressure loss obtained with these two approaches. This point is further investigated in the next section.

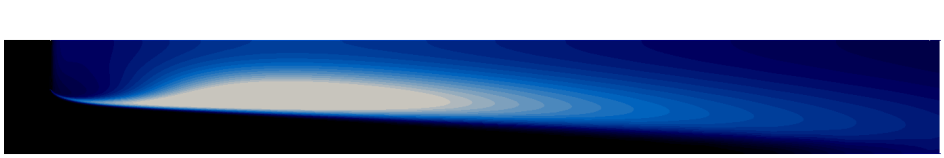

(a) RANS diagonal plane

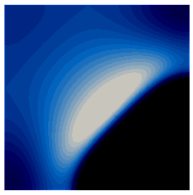

(b) RANS plane $x = d$

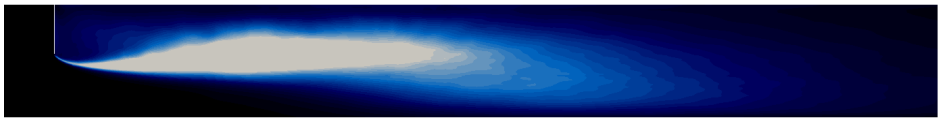

(c) LES diagonal plane

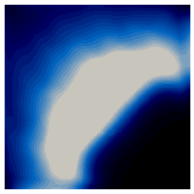

(d) LES plane $x = d$

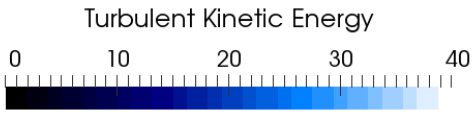

Fig. 7 Cuts of the turbulent kinetic energy field TKE.

D. Pressure loss and sensitivity to the inlet velocity profile

To assess the ability of Star-CCM+ and IC3 to accurately predict the pressure loss, results obtained from numerical solutions are compared to the experimental results of [16]. Since the inlet velocity profile is not known in the experiment, various simulations are performed with varying inlet velocity profiles. To begin with, five different profiles are tested in RANS simulations. A flat profile given by:

$$U_x(y,z) = U_{in}, \tag{1}$$

three power-law profiles given by:

$$U_x(y,z) = \frac{1}{2}\left[\frac{n+1}{n}\,U_{in}\,\left(1-\frac{y}{h}\right)^{1/n} + \frac{n+1}{n}\,U_{in}\,\left(1-\frac{z}{h}\right)^{1/n}\right], \quad n = 2,5,7 \tag{2}$$

and a Poiseuille profile given by:

$$Poiseuille: U_x(y,z) = \frac{1}{2}\left[\frac{3}{2}\,U_{in}\,\left(1-\frac{y^2}{h^2}\right) + \frac{3}{2}\,U_{in}\,\left(1-\frac{z^2}{h^2}\right)\right]. \tag{3}$$

The duct bulk velocity U_{in} remains unchanged for all the cases as well as the associated mass flow rate (incompressible formulation).

The spatial evolution of the dimensionless static pressure along the channel is plotted in Fig. 8 for two different locations. The first line corresponds to the centerline of the duct whereas the second one is located along the channel walls in the symmetry plane. The latter corresponds to the location where measurements are performed in [16] (■ in Fig. 8). However, these numerical and experimental results are not perfectly comparable: in the simulations, pressure losses are reduced to the pressure drop induced by the orifice (duct walls are prescribed with slip conditions) whereas both the orifice contribution and the linear pressure loss caused by fluid-wall friction are encompassed in the experiment. To isolate the singular pressure drop associated with the orifice, k_{GAN}, from the global losses, Gan et al. performed a linear extrapolation of the dimensionless pressure distribution from upstream and downstream to the constriction (— in Fig. 8).

The centerline values and the ones extracted at the mid-wall lead to the same conclusions. The five inlet velocity profiles lead to a similar shape of the pressure distribution along the duct: the pressure minimum and recovery point

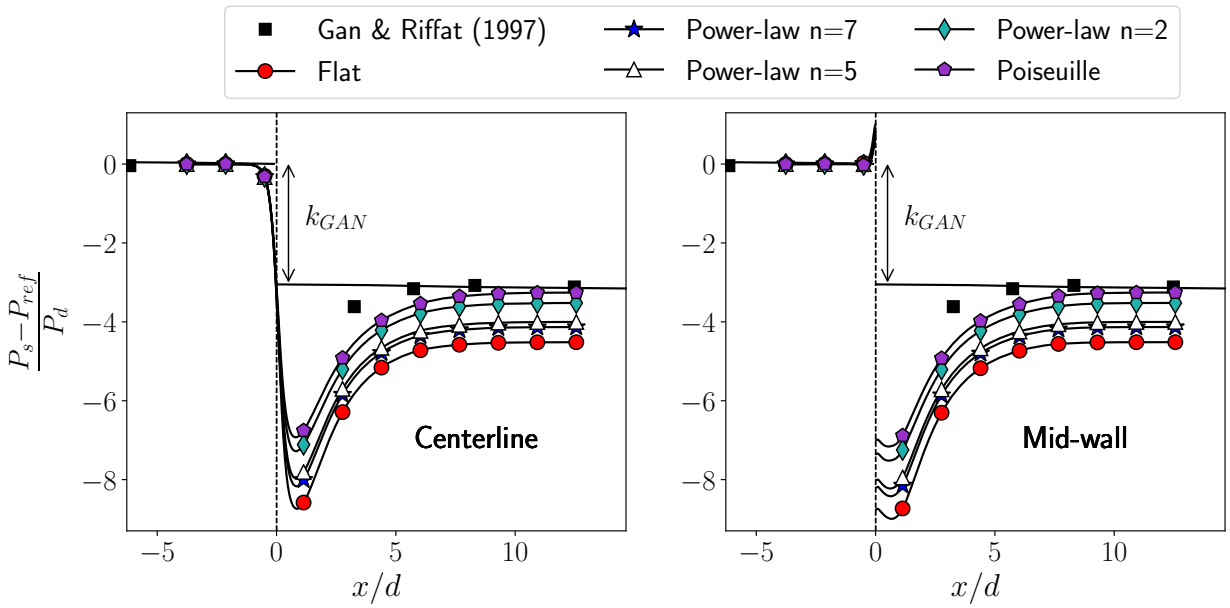

Fig. 8 Spatial evolution of the dimensionless static pressure along the duct for various inlet velocity profiles.

locations remain unchanged. However, variations of pressure levels downstream of the orifice are observed. The more the profile is deformed compared to the flat profile, the smaller the orifice pressure loss is. Note that, this observation agrees with the conclusions of [12] and [13]. The shape of the profile has also a significant effect on the pressure drop: the power-law profile $n = 2$ and the Poiseuille profile present the same maximum velocity but different shapes that lead to a smaller pressure drop with the Poiseuille profile. Finally, in terms of pressure loss level, the results obtained with the Poiseuille profile compare well with experimental data. There is also satisfying agreement regarding the static pressure distribution, however, recompression downstream of the orifice, is slower in RANS computations compared to experimental values. Interestingly, the pressure drop evolution as a function of profile deformation is monotonous with "extremas" obtained for the flat and the Poiseuille profiles. This result is of special interest for the vent flap problem. Indeed, in the industrial configuration, the inlet profile is not known. Regarding the present observation, a results "envelope" could be determined by assuming that the real case lies somewhere between the results obtained for a flat and a Poiseuille profile.

These two cases are then computed with the LES solver. Corresponding results are presented in Fig. 9. For each case, RANS and LES curves are close. The pressure rise downstream of the orifice is, however, faster in LES. This result leads to better agreement of the LES solution with the experimental values which is consistent with the upstream shift of the velocity and turbulent kinetic energy fields observed in Figs. 5 and 7. Nevertheless, the pressure level eventually reached far downstream of the orifice is similar with both numerical approaches. Turbulence drives the flow distribution downstream of the orifice and hence the recompression but has, in the end, a reduced effect on the orifice pressure drop.

To better quantify the comparison between numerical and experimental results, the orifice pressure loss coefficient k is computed for each case and given in Table 2, as well as the relative error when compared to measured values. This coefficient is given by:

$$k = \frac{\Delta P_s}{P_d} \tag{4}$$

where

- $\Delta P_s = P_s^{inlet} - P_s^{outlet}$ is the static pressure difference between inlet and outlet
- $P_d = \frac{1}{2}\rho U^2$ is the dynamic pressure, where U is the bulk velocity in the duct.

As previously observed in Fig. 8, the error decreases when profile deformation increases. The pressure loss coefficient obtained with a Poiseuille inlet velocity profile is the lower and coincides with that obtained in the experiment. Moreover, pressure loss results obtained with RANS and LES are close. In particular, a variation of 3.4% is found when a Poiseuille profile is prescibed at the inlet which is lower than the measurement uncertainties estimated in [16]. Following

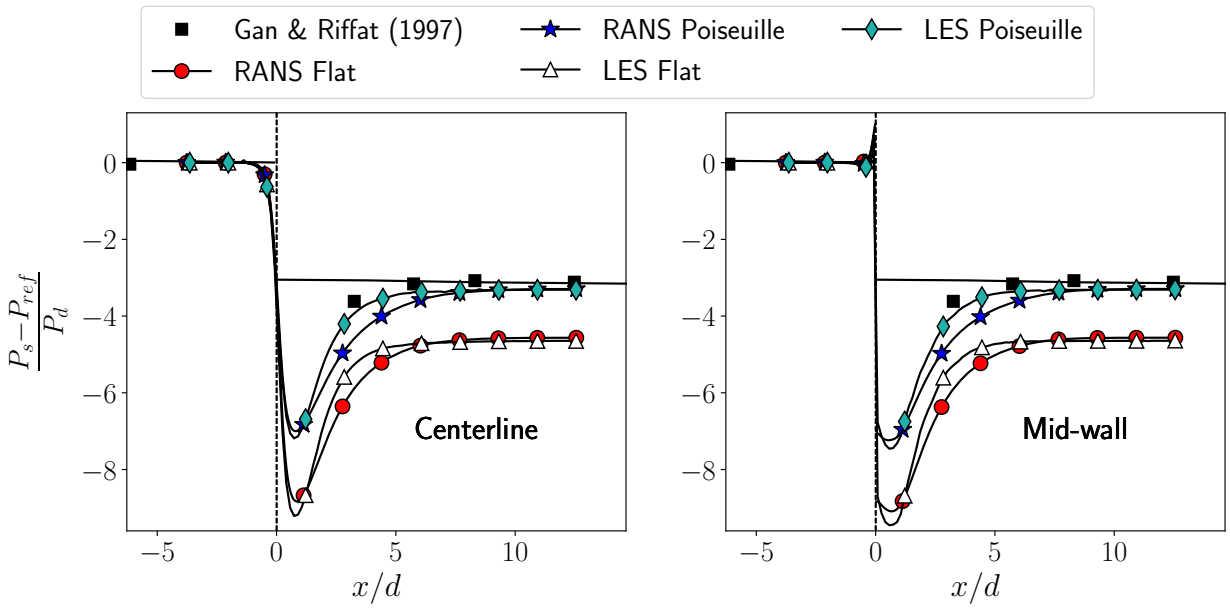

Fig. 9 Spatial evolution of the dimensionless static pressure along the duct obtained with RANS and LES approaches for flat and Poiseuille inlet velocity profiles.

	Target	Flat	1/7	1/5	1/2	Poiseuille
RANS k	3.26	4.52	4.13	4.0	3.52	3.26
RANS Error (%)	-	38.7	26.8	22.8	8.1	0
LES k	3.26	4.65	-	-	-	3.37
LES Error (%)	-	42.7	-	-	-	3.4

Table 2 Pressure loss coefficient k and relative error between numerical and experimental results.

investigations relies hence on solutions obtained with the RANS solver Star-CCM+.

The reference configuration has allowed to confirm the accuracy of the pressure loss predicted numerically and has evidenced the significant influence of the inlet velocity profile on the results. Note however that the geometry of the vent flap problem is different since the jet does not discharge into a confined duct but rather into an open atmosphere (ground testing conditions for certification) or in a transverse freestream (flight conditions). Such unconfined configurations are hence the focus point of the next section.

IV. unconfined configurations

Two different unconfined configurations are studied in order to progress towards the industrial problem. Both geometries are derived from the reference configuration discussed in the previous section (III). As in Section III, the geometries as well as the numerics of the solver are detailed. An analysis of the pressure loss and discharge performance is then presented for two different situations: when the jet discharges either into an open atmosphere or in a transverse freestream.

A. Configurations and numerical setup

Both unconfined configurations are illustrated in Fig. 2. The orifice-unconfined configuration (Fig. 2b) is obtained by replacing the downstream part of the duct of the reference configuration by an open atmosphere. The latter is featured in the simulation by a large rectangular box (Fig. 10) which dimensions are $Lx = 21d$ by $Ly = 42d$ by $Lz = 42d$. All

other dimensions (orifice, upstream duct etc) remain unchanged from the reference configuration.

Inlet and upstream duct boundary conditions are set in the same manner as for the reference configuration. Likewise, the upstream wall of the orifice plate as well as the orifice wall conditions are kept to non slip walls (Fig. 10). The downstream box boundary conditions are then set with two different manners, depending on whether the jet discharges to an open atmosphere (without cross flow) or in a transverse freestream (with cross flow). In the first case, to mimic the open atmosphere, all boundaries except the one adjacent to the orifice plate are outlet conditions at atmospheric pressure (Fig. 10 left). For the second case, when a cross flow is included in the simulation, the lower boundary condition of the bow is switched from an outlet to a uniform velocity inlet and boundaries normal to the z axis are set to symmetry conditions (Fig. 10 right). In both cases, the downstream wall of the orifice plate is set with a slip condition to prevent any boundary layer development along this wall (Fig. 10).

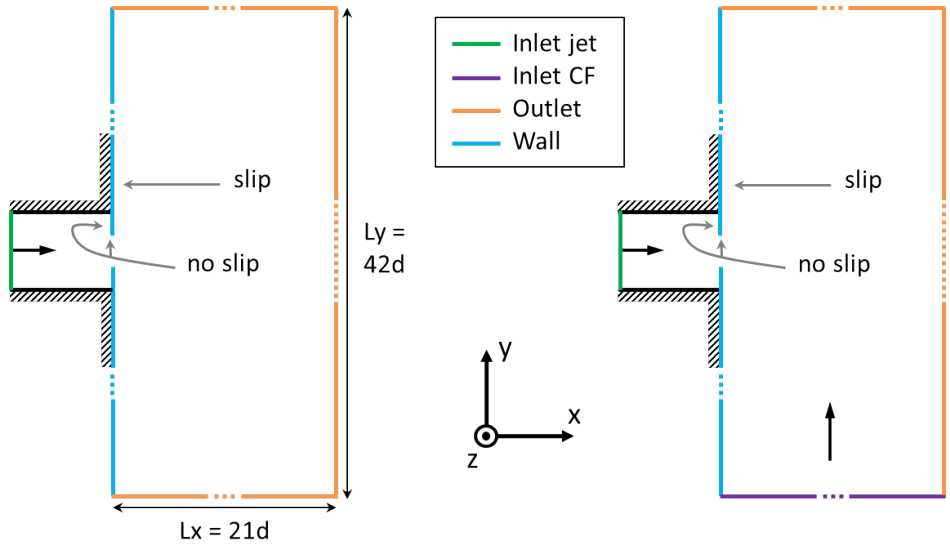

Fig. 10 Boundary conditions for unconfined configurations illustrated on the orifice-unconfined case. Jet discharging into an open atmosphere (without cross flow, left) and in a transverse freestream (with cross flow, right)

The Jet In Cross Flow (JICF) configuration is derived from the orifice-unconfined configuration. The original upstream duct is suppressed and the orifice surface is extruded in the upstream direction to match the original upstream duct length (Fig. 2c). All boundary conditions but the jet inlet are retained from the orifice-configuration. To set the jet inlet profile, the axial velocity values are extracted at the orifice in the orifice-unconfined case without cross flow. The resulting velocity profile is then imposed at the inlet of the JICF simulation.

Numerical parameters are kept unchanged from the reference configuration computation. Mesh size and topology are also directly inherited from the results of the mesh convergence study performed on the reference configuration.

B. Flow and pressure loss in confined and unconfined configurations (without cross flow)

1. Comparison of the confined and the unconfined flows

The flow solution obtained for the orifice-unconfined configuration is analyzed and compared to the flow field obtained with the reference configuration. Both simulations are run with a Poiseuille velocity profile at the inlet. As in Figs. 5 and 7, the flow fields are displayed on two different 2D cuts: the diagonal plane that passes through the origin, and an axial cut located one diameter downstream of the orifice ($x = d$).

Figure 11 shows axial velocity fields U_x obtained with the reference and orifice-unconfined configurations in the

two cut planes along with zero axial velocity contours. Figures 11a and 11c depict identical flow features upstream of the orifice in both configurations. In particular, zero velocity contours locations in that region are the same. On the other hand, the contours show different recirculation zones downstream of the orifice. While well developed in the reference configuration, the recirculation zone reduces to a small dead flow zone very close to the orifice in the unconfined configuration. Another difference lies in the axial extent of the jet core which is almost one third longer in the unconfined case. The $x = d$ plane (Figures 11b and 11d) exhibits similar flow fields for both configurations. However, some discrepancies appear along the diagonal of the plane: while the jet flattens under the action of the recirculation zone in Fig. 11b (confined), the opposite phenomenon is observed in Fig. 11d (unconfined), where the flow spreads towards the corner. Note that the jet flattening effect in the reference configuration has previously been shown in Fig. 5b and 5d. Finally, the angle of spread obtained in the unconfined configuration simulation (not shown) is consistent with the freejet theory [24].

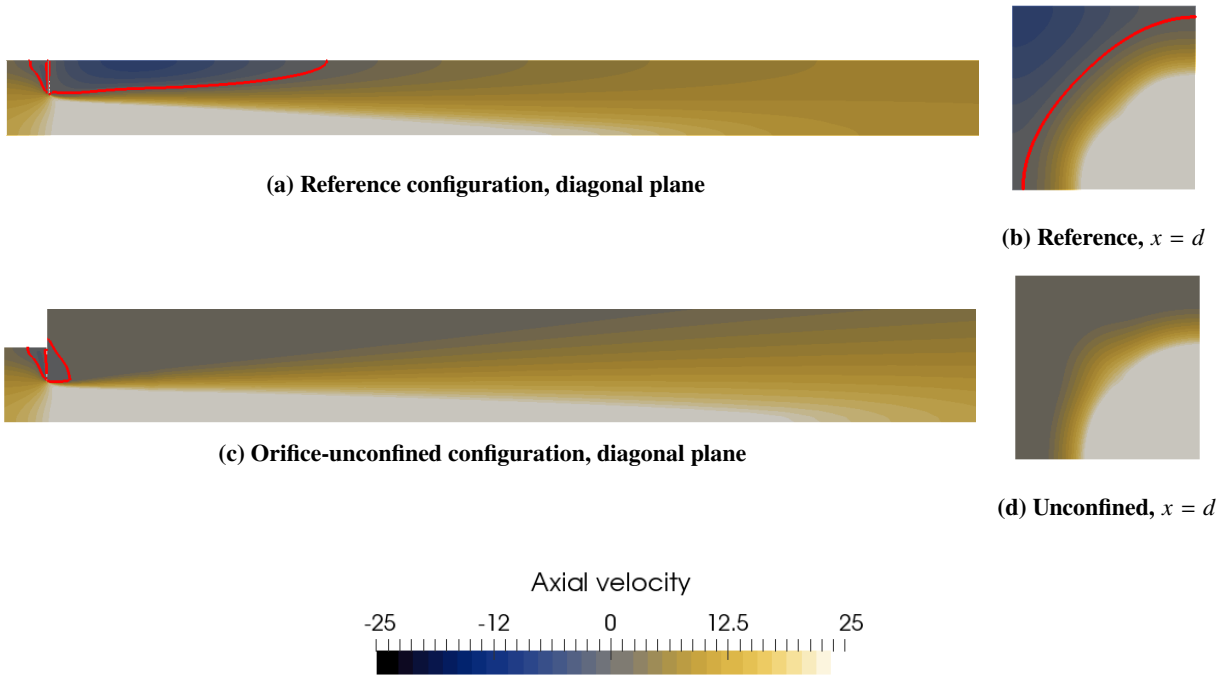

(a) Reference configuration, diagonal plane

(b) Reference, $x = d$

(c) Orifice-unconfined configuration, diagonal plane

(d) Unconfined, $x = d$

Fig. 11 Cuts of the axial velocity field U_x and zero axial velocity contours (in red).

Differences in flow topology obtained in the confined and unconfined configurations are better quantified in Fig. 12 which presents axial velocity profiles at various locations along the diagonal plane. Both simulations provide the same velocity profiles up to the downstream wall of the orifice (located at $x = 0.002$). At $x = 0.1d$, both axial velocity profiles are similar in the jet zone and differences result exclusively from the absence of a recirculation zone in the unconfined configuration. Further downstream, differences arise on the jet shape: the latter is slightly wider in the unconfined configuration compared to the reference one and depicts a larger axial velocity magnitude in the whole jet extent ($x = 3d$). Far from the orifice, at $x = 12d$, while the axial velocity is now uniform in the confined case, a deformed profile is still observed in the unconfined configuration. In this latter case, the jet is not constrained and only slows down due to jet spreading and dissipation. Note that the unconfined axial velocity profile evolves following the freejet theory: the initially squared jet core rounds and flattens as the jet spreads [24].

As shown in Fig. 13, the two configurations result in different turbulent kinetic energy fields. Turbulence is mostly produced by the strong interaction between the jet and the recirculation zone in the reference configuration whereas in the unconfined case, turbulence develops as the jet spreads. The absence of a large recirculation zone leads to lower values of the TKE in the unconfined configuration. The peak value is reduced by 40% and is located further downstream compared to the reference configuration.

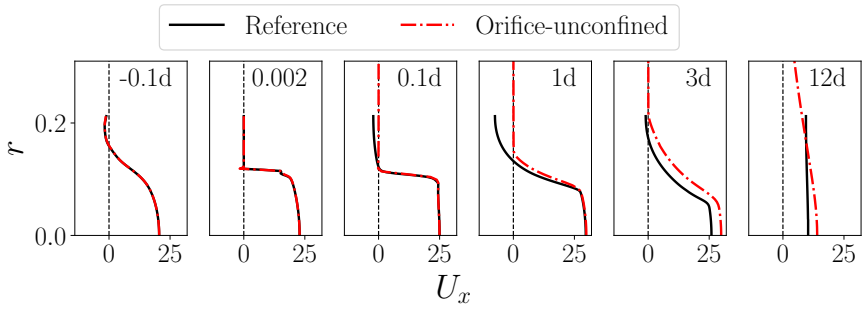

Fig. 12 Axial velocity U_x profiles in the diagonal plane, at various axial locations.

(a) Reference configuration, diagonal plane

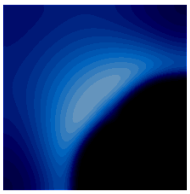

(b) Reference, $x = d$

(c) Orifice-unconfined configuration, diagonal plane

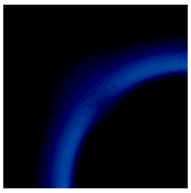

(d) Unconfined, $x = d$

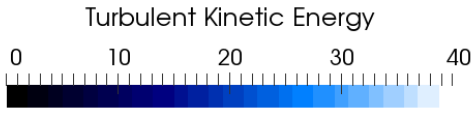

Fig. 13 Cuts of the turbulent kinetic energy field TKE.

2. Pressure loss in confined and unconfined configurations

Since the quantity of interest for the vent flap application is the effective air quantity discharged through the orifice, performance is no longer evaluated using the pressure loss coefficient. Instead, the discharge coefficient is used. The latter is the ratio between the effective mass flow rate extracted from experiments or computations and the theoretical ideal (isentropic) mass flow rate:

$$C_d = \frac{\dot{m}_{eff}}{\dot{m}_{ideal}} = \int_S \rho U_x dS \times \frac{1}{S\sqrt{2\rho\Delta P}} \tag{5}$$

where

- $\dot{m}_{eff}$ is the effective mass flow rate extracted from the simulation
- $\dot{m}_{ideal} = S\sqrt{2\rho\Delta P}$ is the ideal isentropic mass flow rate (computed here with an incompressibility assumption)
- U_x is the axial velocity
- S is the orifice area
- $\Delta P = P_t^{inlet} - P_s^{outlet}$ is the difference between inlet total pressure and outlet static pressure.

Figures 14 and 15, display variations of the discharge coefficient with jet Reynolds number and inlet velocity profile respectively. Jet Reynolds number values for the reference configuration have been chosen to reproduce the ones from

[16], while in the unconfined case, these have been arbitrarily chosen to be equal to the baseline jet Reynolds number ($Re_{jet} = 3.2 \times 10^5$) times 1, 1/3 and 3 respectively. Results show (Fig. 14) that the discharge coefficient does not depend

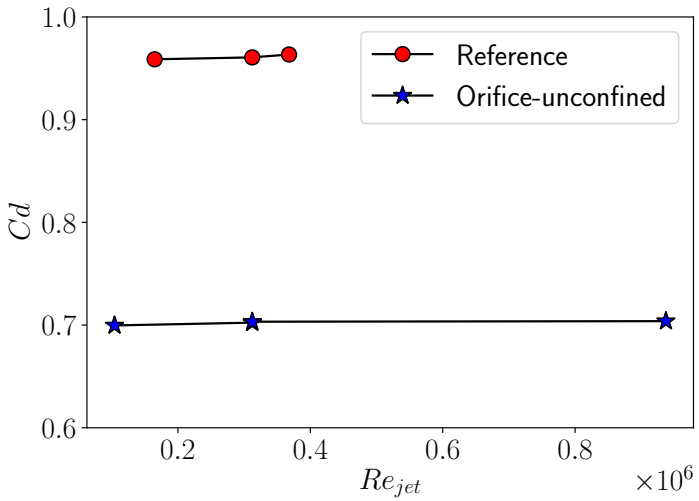

Fig. 14 Discharge coefficient variation with jet Reynolds number for the reference and orifice-unconfined configurations (without cross flow).

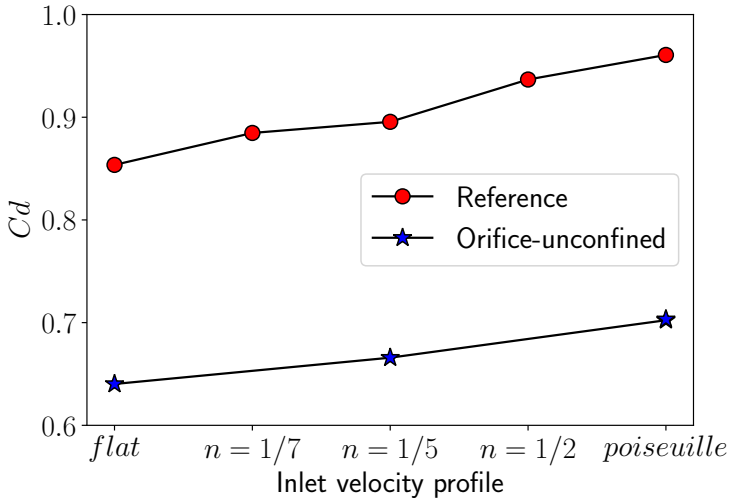

Fig. 15 Discharge coefficient variation with inlet velocity profile for the reference and orifice-unconfined configurations (without cross flow).

on the jet Reynolds number for both configurations. However, as in Fig. 8, Fig. 15 shows that discharge performance is affected by the inlet velocity profile. The confined and unconfined cases coefficients vary in the same manner with inlet velocity profile deformation. The larger discharge coefficient is obtained in both cases for a Poiseuille profile because the latter is associated with lower pressure losses as shown in Fig. 8 for the reference configuration.

The interesting conclusion from these results lies in the fact that while pressure loss and discharge flow correlation usually take the Reynolds number as an input, the influence of the inlet velocity profile is rarely included. Instead, correlations are mostly provided assuming, for example, a perfectly developed flow [25]. While such an assumption is practicable in well controlled facilities, high uncertainties remain on the inlet velocity profile in many industrial applications, like in the case of aircraft door vent flaps.

C. Cross flow effects on pressure loss

Outlet discharge performance is then assessed for cases with a transverse freestream. Five different values of the velocity ratio R_v between the jet U_{jet} and the cross flow U_{CF} ranging from 0.2 to 5 are investigated. For all five cases, the jet and the cross flow Mach numbers are below 0.3, ensuring the validity of the incompressible assumption used for the computations. Moreover, since the fluid density is constant all over the domain, the velocity ratio and the mass flow ratio are equivalent. Several computations are performed with different U_{CF}, while U_{in} and thus U_{jet} are kept constant and equal to the baseline values used throughout this paper. A Poiseuille profile is prescribed at the duct inlet while the cross flow velocity is set with a flat profile. Two different configurations are reported here: the orifice-unconfined configuration (Fig. 2b) and the JICF case (Fig. 2c).

For each configuration and velocity ratio, the axial velocity field is displayed in Fig. 16 in the $z = 0$ plane (cross flow comes from the lower side). Note that only a reduced part of the domain is shown here. The outlet jet is deviated by the

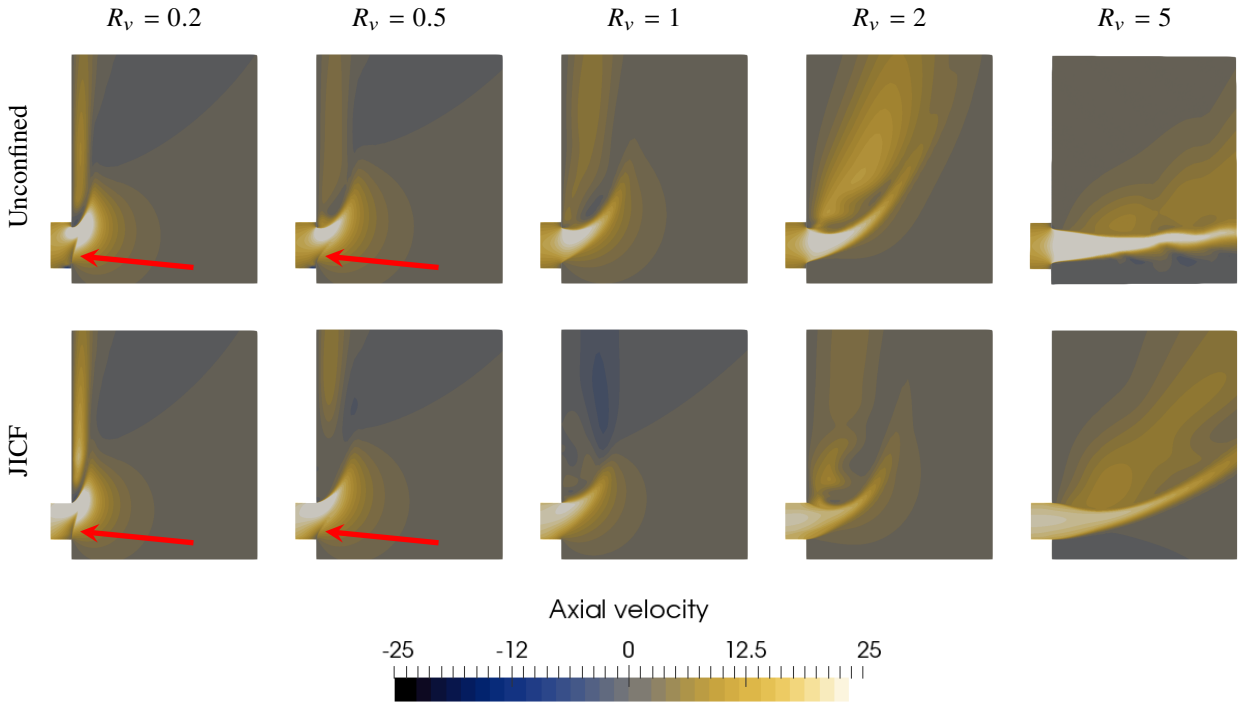

Fig. 16 $Z = 0$ cuts of the axial velocity field U_x (cross flow comes from the lower side). The red arrow points towards the stagnation line.

cross flow in all cases but the deviation magnitude varies with the configuration and the velocity ratio. For $R_v = 0.2$ and $R_v = 0.5$, jet deviation is strong. Interaction between the two flows forms a stagnation line: a null velocity line going from the lower side of the outlet towards the centerline and which location is indicated with a red arrow in Fig. 16. Its length is similar for both configurations but decreases when R_v increases. The stagnation line imposes a section restriction to the jet flow which is hence deviated towards the outlet upper side. For these low velocity ratio cases, results obtained with the orifice-unconfined and JICF configurations are very similar.

As the velocity ratio is further increased, the stagnation line vanishes and differences arise between the two configurations. In particular, jet deviation is stronger in the JICF configuration compared to the unconfined case. One physical explanation is that the orifice modifies the two jet interaction and partially protects the jet from the cross flow influence. In addition, part of this effect could come from differences in the jet velocity profile at the outlet. Indeed, even if the orifice profile is prescribed at the duct inlet in JICF computations (to best mimic the profile of the unconfined case), the abrupt profile set at the inlet (zero velocity at the wall and deformed profile) smoothes in the approach duct as it approaches the outlet. As evidenced in the previous section, profile differences impact the flow field as well as the pressure loss, and as low as the differences might be between the two cases, this could explain certain differences in the flow fields. Finally, additional patterns of moderate axial velocity are visible for both configurations when $R_v = 2$ and

$R_v = 5$. These corresponds to the jet oscillation as well as recirculations between the curved jet and the wall.

Figure 17 presents variations of the discharge coefficient with R_v for both configurations as well as the value obtained without cross flow which is conceptually equivalent to the limit case when $R_v \sim \infty$. Both configurations curves follow the same global evolution: C_d increases with the velocity ratio up to $R_v = 2$ and then decreases, evidencing optimal operating conditions for which C_d is maximum. For $R_v = 0.2$ and $R_v = 0.5$, discharge coefficients are low and very close for both configurations, JICF values being less than 6% higher than the ones obtained for the unconfined configuration. As evidenced in Fig. 17, for low velocity ratio cases, the transverse freestream strongly restricts the jet flow section, thereby decreasing the outlet performance. As a result, outlet geometry variations between the two configurations barely impact the pressure loss, which is instead controlled by the cross flow. When $R_v > 0.5$, the difference between the two configurations increases with velocity ratio and reaches 50% of the orifice-unconfined value for $R_v = 5$. As R_v increases the pressure loss induced by the cross flow decreases and the orifice contribution to the total pressure loss is more and more significant.

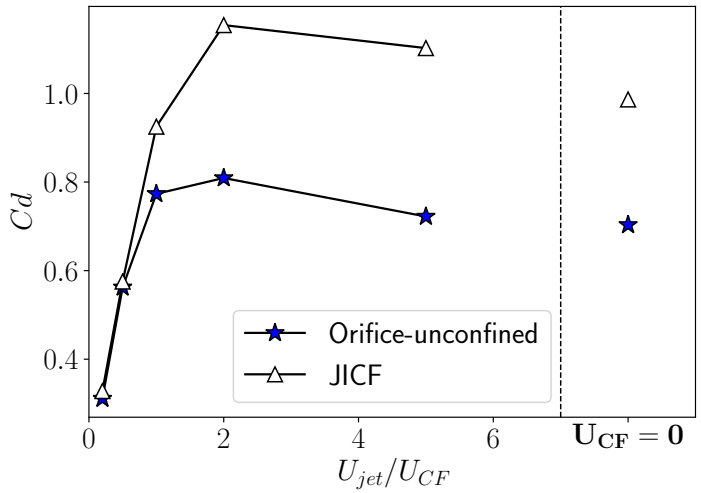

Fig. 17 Discharge coefficient variation with velocity ratio between jet and cross flow for orifice-unconfined and JICF configurations.

Moreover, the discharge coefficient obtained with cross flow exceeds that of the freejet ($U_{CF} = 0$) for several operating conditions. Such flow behavior has been observed in [2] as well as in turbine film cooling holes [7]. For the latter case, a detailed study of the phenomenon [26] led to the conclusion that the enhanced discharge coefficient comes from the combination of a locally reduced static pressure at the hole outlet and the jet entrainment by the freestream. Consequently, the discharge coefficient associated with the JICF configuration exceeds 1 (i.e. real mass flow rate overtakes the isentropic theoretical value) for $R_v = 2$ and $R_v = 5$.

C_d orders of magnitude as well as curve evolution tendencies highlighted here match well with experimental results presented in [2] and [3] on the mass flow ratio range investigated in the experiments (corresponding to $R_v < 1$). Even if direct comparison is not relevant, since Reynolds and Mach numbers as well as inlet velocity profile or cross flow boundary are not comparable, the global features previously mentioned here are also supported by the experiments. Moreover, the present study suggests an optimal C_d value for $R_v = 2$ whereas the range of mass flow ratio investigated experimentally for round orifices is below < 0.9 [2]. As a result, the existence of an optimum in the C_d curve is not shown in the experiment. However, such an optimum has been observed at low mass flow ratios in [3] for high aspect ratio rectangular orifices. Such configurations are not discussed in the present paper but are currently under investigation by the authors.

The evidence of an optimum discharge coefficient for a velocity ratio around $R_v = 2$ with a round orifice is the key result of the present study, which opens the way for optimal design of industrial vent flaps. Based on current designs, whatever the operating conditions, R_v is generally below 0.6, resulting in quite low discharge coefficients. A reduction of outlet sizes would accelerate the jet flow and hence increase velocity ratios. This could lead to better discharge performance, while reducing the size of the opening and therefore reduce the constraints on overall equipment design.

V. Conclusion

A reference configuration for which experimental pressure loss data are available in the literature has first been studied using a RANS and a LES solver. Despite some differences in the flow dynamics observed downstream of the orifice, the pressure drop predicted with both numerical approaches is very similar. In both cases, a steady decrease of the orifice pressure loss is observed as the duct inlet velocity profile is varied from a flat profile to a Poiseuille profile. In addition, the numerical data compares well with experimental values when such a profile is prescribed.

The reference configuration is then modified to an unconfined geometry. First, without cross flow, and in both confined and unconfined configurations, the inlet velocity profile is a key parameter in discharge coefficient value while the jet Reynolds number influence is negligible on the range investigated. This result is of particular interest for industrial applications where the inlet velocity profile is usually not known.

As a second step, a transverse flow with varying velocity is included in the computations and discharge coefficient values are compared between an unconfined configuration with an orifice and a classic Jet In Cross Flow (JICF) case. For low velocity ratios, the outlet performance is low. Interaction between the jet and the cross flow imposes a strong section restriction to the jet which is responsible for most of the pressure loss and leads to very similar values of discharge coefficient in both configurations. Differences between the two configurations increase with the velocity ratio. Moreover, both curves evidence an optimal operating condition for which C_d is maximum and exceeds the freejet value. The evidence of such an optimum value of the discharge coefficient for high velocity ratios in round orifice configurations is the main result of the present study. A similar optimum has been observed at lower velocity ratios for high aspect ratio rectangular outlets in [3]. This, as well as the impact of including the mobile vent panel in the simulations, is currently investigated by the authors.

References

[1] Job, M., *Air Disaster*, No. vol.1 in Air Disaster, Aerospace Publications, 1994.

[2] Nelson, W., and Dewey, P., "A Transonic Investigation of the Aerodynamic Characteristics of Plate- and Bell- Type Outlets for Auxiliary Air," Tech. rep., NACA-RM-L52H20, 1952.

[3] Dewey, P., and Vick, A., "An Investigation of the Discharge and Drag Characteristics of Auxilliary-air Outlets Discharging into a Transonic Stream," Tech. rep., NACA-TN-3466, 1955.

[4] Batista De Jesus, A., Takase, V. L., and Vinagre, H. T. M., "CFD Evaluation of the Discharge Coefficient of Air Outlets In the Presence of an External Flow," *Proceedings of the 10th Brazilian Congress of Thermal Sciences and Engineering*, 2004.

[5] Mahesh, K., "The Interaction of Jets with Crossflow," *Annual Review of Fluid Mechanics*, Vol. 45, No. 1, 2013, pp. 379–407.

[6] Hay, N., Lampard, D., and Benmansour, S., "Effect of Crossflows on the Discharge Coefficient of Film Cooling Holes," *Journal of Engineering for Power*, Vol. 105, No. 2, 1983, pp. 243–248.

[7] Rowbury, D. A., Oldfield, M. L. G., and Lock, G. D., "Engine Representative Discharge Coefficients Measured in an Annular Nozzle Guide Vane Cascade," *ASME International Gas Turbine and Aeroengine Congress and Exhibition*, 1997, pp. 1–8.

[8] Burd, S. W., and Simon, T. W., "Measurements of Discharge Coefficients in Film Cooling," *Journal of Turbomachinery*, Vol. 121, No. 2, 1999, pp. 243–248.

[9] Gritsch, M., Schulz, A., and Wittig, S., "Effect of Crossflows on the Discharge Coefficient of Film Cooling Holes With Varying Angles of Inclination and Orientation," *Journal of Turbomachinery*, Vol. 123, No. 4, 2001, pp. 781–787.

[10] Irving, S., "The effect of disturbed flow conditions on the discharge coefficient of orifice plates," *International Journal of Heat and Fluid Flow*, Vol. 1, No. 1, 1979, pp. 5–11.

[11] Morrison, G., DeOtte, R., and Beam, E., "Installation effects upon orifice flowmeters," *Flow Measurement and Instrumentation*, Vol. 3, No. 2, 1992, pp. 89–93.

[12] Morrison, G. L., Panak, D. L., and DeOtte, R. E., "Numerical Study of the Effects of Upstream Flow Condition Upon Orifice Flow Meter Performance," *Journal of Offshore Mechanics and Arctic Engineering*, Vol. 115, No. 4, 1993, pp. 213–218.

[13] Morrison, G. L., Hall, K. R., Macek, M. L., Ihfe, L. M., DeOtte, R. E., and Hauglie, J. E., "Upstream velocity profile effects on orifice flowmeters," *Flow Measurement and Instrumentation*, Vol. 5, No. 2, 1994, pp. 87–92.

[14] Branch, J. C., "The effects of an upstream short radius elbow and pressure tap location on orifice discharge coefficients," *Flow Measurement and Instrumentation*, Vol. 6, No. 3, 1995, pp. 157–162.

[15] Zimmermann, H., "Examination of disturbed pipe flow and its effects on flow measurement using orifice plates," *Flow Measurement and Instrumentation*, Vol. 10, No. 4, 1999, pp. 223–240.

[16] Gan, G., and Riffat, S. B., "Pressure loss characteristics of orifice and perforated plates," *Experimental Thermal and Fluid Science*, Vol. 14, No. 2, 1997, pp. 160–165.

[17] Star-CCM+, "https://mdx.plm.automation.siemens.com/star-ccm-plus," , 2019.

[18] Wilcox, D. C., "Reassessment of the scale-determining equation for advanced turbulence models," *AIAA Journal*, Vol. 26, No. 11, 1988, pp. 1299–1310.

[19] Menter, F. R., "Two-equation eddy-viscosity turbulence models for engineering applications," *AIAA Journal*, Vol. 32, No. 8, 1994, pp. 1598–1605.

[20] Jones, W. P., and Launder, B. E., "The Prediction of Laminarization with a Two-Equation Model of Turbulence," *International Journal of Heat and Mass Transfer*, Vol. 15, 1972, pp. 301–314.

[21] Durbin, P. A., "Near-wall turbulence closure modeling without "damping functions"," *Theoretical and Computational Fluid Dynamics*, Vol. 3, No. 1, 1991, pp. 1–13.

[22] Spalart, P., and Allmaras, S., "A one-equation turbulence model for aerodynamic flows," *30th Aerospace Sciences Meeting and Exhibit*, 1992.

[23] Vreman, A. W., "An eddy-viscosity subgrid-scale model for turbulent shear flow: Algebraic theory and applications," *Physics of Fluids*, Vol. 16, No. 10, 2004, pp. 3670–3681.

[24] Pope, S. B., *Turbulent Flows*, Cambridge University Press, 2000.

[25] Reader-Harris, M., Sattary, J., and Spearman, E., "The orifice plate discharge coefficient equation — further work," *Flow Measurement and Instrumentation*, Vol. 6, No. 2, 1995, pp. 101–114.

[26] Rowbury, D. A., Oldfield, M. L. G., and Lock, G. D., "Large-Scale Testing to Validate the Influence of External Crossflow on the Discharge Coefficients of Film Cooling Holes," *Journal of Turbomachinery*, Vol. 123, No. 3, 2001, pp. 593–600.